



Effects of composition faults in ternary metal chalcogenides ($Zn_xIn_2S_{3+x}$, $x = 1\text{--}5$) layered crystals for visible-light-driven catalytic hydrogen generation and carbon dioxide reduction

Yan Wu^a, Hou Wang^{a,*}, Wenguang Tu^a, Shuyang Wu^a, Jia Wei Chew^{a,b,*}

^a School of Chemical and Biomedical Engineering, Nanyang Technological University, Singapore 637459, Singapore

^b Singapore Membrane Technology Center, Nanyang Environment and Water Research Institute, Nanyang Technological University, Singapore 639798, Singapore



ARTICLE INFO

Keywords:
 $ZnxIn_2S_{3+x}$
Composition faults
Photocatalysis
Water splitting
CO₂ reduction

ABSTRACT

Exploring efficient and stable photocatalysts is critical for the practical application of photocatalytic water splitting to get clean hydrogen fuel. In this work, $Zn_xIn_2S_{3+x}$ ($x = 1\text{--}5$) samples with various composition faults were synthesized through a simple hydrothermal method as a series of highly efficient visible-light-driven photocatalysts. Composition faults in $Zn_xIn_2S_{3+x}$ samples played important roles in the charge carrier transfer from internal to external surfaces, further affecting the redox reaction of photogenerated electrons and holes at the solid-liquid interface. The absorption edge of $Zn_xIn_2S_{3+x}$ samples shifted to shorter wavelengths as the atomic ratio of Zn/In in the synthetic solution was increased (i.e., x increased from 1 to 5). The photocatalytic activity of $Zn_xIn_2S_{3+x}$ was evaluated via photocatalytic hydrogen production from water and CO₂ reduction under visible light irradiation. The obtained $ZnIn_2S_4$ ($x = 1$) sample displayed the best photocatalytic activity among the $Zn_xIn_2S_{3+x}$ photocatalysts, with the hydrogen evolution rate determined to be $2.93 \text{ mmol h}^{-1} \text{ g}^{-1}$ and the quantum yield at 420 nm determined to be 7.92%. As for visible light-driven CO₂ reduction, the $ZnIn_2S_4$ sample also exhibited the highest CO formation rate of $40.4 \text{ } \mu\text{mol h}^{-1} \text{ g}^{-1}$. Results suggest that the existence of composition faults provided extra energy barriers to block photoinduced charge carrier transfer. Furthermore, the cyclic tests indicate the stability of the $ZnIn_2S_4$ product over five cycles of repeated use. This study provides new insights into unveiling the relationship of structure-property of $Zn_xIn_2S_{3+x}$ layered crystals, which are valuable for implementation in a wide range of environmental energy applications.

1. Introduction

Solar-driven hydrogen evolution, as green and environmentally friendly resources, is considered an attractive and promising strategy to solve the increasingly critical energy and environmental issues [1–3]. To date, numerous efforts have been made to design highly efficient semiconductor photocatalysts for hydrogen generation [4–7]. A range of visible-light responsive semiconductor photocatalysts, such as metal oxide, metal sulfide, metal-free organic semiconductor and metal-organic framework, have been extensively investigated [8–11]. For example, our group introduced CdS nanostructure coated with exfoliated sulfur-doped carbon nitride as a heterogeneous photocatalyst for photocatalytic hydrogen generation in presence of platinum co-catalyst [12]. However, the total photocatalytic reaction rate of water splitting is not satisfactory in most cases, mainly because of the slow separation and migration kinetics of charge carriers [13].

As a new important member in the field of ternary metal chalcogenides, Zn-In-S (the general formula is $Zn_xIn_2S_{3+x}$, $x = 1\text{--}5$) has received much attention for applications such as photocatalysis and energy conversion owing to its appropriate band gaps and band edges, unique electronic structure, and tunable optical properties [14,15]. The two-dimensional nanosheet configuration is beneficial to decrease the diffusion length of charge carriers, expose abundant catalytically active sites, and provide high surface area for heterogeneous photocatalysis. It has been reported that the band gap of $Zn_xIn_2S_{3+x}$ is $2.46\text{--}2.86 \text{ eV}$, which can be employed as visible-light responsive photocatalyst [16]. In order to enhance photocatalytic performance, various strategies have been adopted, including morphology control, heterostructure construction and defects modulation. For example, $ZnIn_2S_4$ sub-microparticles produced high photocatalytic H₂ generation under visible light illumination [17]. In solar-driven CO₂ reduction, the $ZnIn_2S_4$ layer with abundant zinc vacancies demonstrated a CO formation rate of

* Corresponding authors at: School of Chemical and Biomedical Engineering, Nanyang Technological University, Singapore 637459, Singapore.
E-mail addresses: huankewanghou024@163.com (H. Wang), JChew@ntu.edu.sg (J.W. Chew).

$33.2 \mu\text{mol g}^{-1} \text{h}^{-1}$ [18]. Wang et al. reported that heterogeneous structure of $\text{CdS}/\text{ZnIn}_2\text{S}_4$ was successfully synthesized by the solvothermal method and possessed excellent photoelectron-chemical performance [19]. Our previous research also showed that MXene and carbon nitride can be used as cocatalyst to improve the photocatalytic activity of $\text{Zn}_2\text{In}_2\text{S}_5$ and $\text{Zn}_3\text{In}_2\text{S}_6$, respectively, for water splitting to generate hydrogen [11,20]. Very recently, Li et al. demonstrated that the synergistic contribution of the rearranged sulfur vacancies and sulfur interstitials of $\text{Zn}_2\text{In}_2\text{S}_5$ dramatically enhanced for photocatalytic H_2 production activity by 13-fold [21]. However, the structure-properties of $\text{Zn}_x\text{In}_2\text{S}_{3+x}$ materials for photocatalysis can be further explored and enhanced.

In photocatalysis, the three key processes are photoexcitation, charge carrier transfer and interfacial chemical reaction. Among them, the transfer of photoinduced charge carrier from interior to external surface is a rate-determining step dictating photocatalytic performance. The electrical conductivity of $\text{Zn}_x\text{In}_2\text{S}_{3+x}$ is highly anisotropic, and depends on the presence of composition faults between the layers of $\text{Zn}_x\text{In}_2\text{S}_{3+x}$ [22]. The fringe sequence of sulfur-layer structural unit is not completely periodic, but occasionally disturbed by the fringes of different spacing. These interferential layer packets, which deviate in composition from the bulk material, shows up as composition faults. In $\text{Zn}_x\text{In}_2\text{S}_{3+x}$, the composition faults, locally disturbing the periodicity of the crystal, are mainly isolated faults with x -values smaller than the bulk material [23]. The composition faults are listed in Table S1. The composition faults can create potential barriers. Free carriers are able to move freely in all directions between them, but they must pass over or tunnel through the barriers to contribute to the conductivity parallel to the c -axis. Therefore, a small concentration of composition faults (guest layers) disrupts the system conductance, leading to a strong anisotropy across and along the layers [24]. Unfortunately, not much attention has been paid to the effects of composition faults of $\text{Zn}_x\text{In}_2\text{S}_{3+x}$ layered crystals in the field of photocatalytic applications.

Herein, $\text{Zn}_x\text{In}_2\text{S}_{3+x}$ samples with various composition faults were prepared via a simple hydrothermal method and were characterized through a series of characterization techniques. The ZnIn_2S_4 sample displayed the best photocatalytic activity among all the prepared samples. Composition faults in $\text{Zn}_x\text{In}_2\text{S}_{3+x}$ samples played important roles in internal charge transfer, further affecting the redox reactions of photogenerated electrons and holes. The underlying mechanisms are explored via applying photoluminescence spectroscopy, photoelectrochemical measurement and current-voltage curve analysis. A possible reaction mechanism for photocatalytic H_2 generation and CO_2 reduction under the visible-light irradiation was proposed. This study not only unveils the relationship of structure-properties of $\text{Zn}_x\text{In}_2\text{S}_{3+x}$ layered crystals in the field of photocatalytic applications, but also expands the potential applications in the fields of solar energy-fuel conversion.

2. Experimental

2.1. Material preparation

$\text{Zn}_x\text{In}_2\text{S}_{3+x}$ samples were synthesized via a simple hydrothermal method. For each preparation, x mmol ZnCl_2 , 2 mmol $\text{InCl}_3 \cdot 4\text{H}_2\text{O}$ and ($6 + 2x$) mmol thioacetamide (TAA) were dispersed in deionized water (40 mL) and magnetically stirred for 2 h. Then the mixed solution was transferred into the Teflon-lined stainless steel autoclave and maintained at 180°C for 12 h in the electric oven. After naturally cooling to room temperature, the product was collected by centrifugation, washed several times with ethanol and deionized water, and then finally dried in the electric oven at 60°C for 12 h. The as-obtained samples, namely, ZnIn_2S_4 , $\text{Zn}_2\text{In}_2\text{S}_5$, $\text{Zn}_3\text{In}_2\text{S}_6$, $\text{Zn}_4\text{In}_2\text{S}_7$ and $\text{Zn}_5\text{In}_2\text{S}_8$ were denoted as ZIS1, ZIS2, ZIS3, ZIS4 and ZIS5, respectively. For comparison, In_2S_3 was also prepared via a similar method as that for the preparation of $\text{Zn}_x\text{In}_2\text{S}_{3+x}$, but without adding ZnCl_2 in the synthesis process. The

detailed material characterization is described in the Supporting Information.

2.2. Photocatalytic H_2 evolution

The photocatalytic H_2 production capacity is a crucial indicator of photocatalytic activity. In detail, 50 mg of above synthesized $\text{Zn}_x\text{In}_2\text{S}_{3+x}$ samples were suspended in 100 mL of a mixed solvent $\text{H}_2\text{O}/\text{TEOA}$ (85:15 v/v). Then, required stoichiometric amount of $\text{H}_2\text{PtCl}_6 \cdot 6\text{H}_2\text{O}$ (i.e., 1, 2, 3 and 5 wt% of Pt) were added to the above suspension. A 250 mL top-illuminated quartz reaction vessel was connected to the closed glass gas recirculation system, and the 300 W Xenon lamp was employed as the light source, with the cut-off filter employed to produce visible light ($\lambda > 420 \text{ nm}$). Before photoreaction, the system was evacuated to completely remove air as well as dissolved oxygen. The reaction temperature was kept at the room temperature via a cooling water circulation system, and the cumulative amount of generated gases was detected in-situ every 1 h interval employing the gas chromatograph equipped with thermal conductive detector (TCD).

The apparent quantum yield (AQY) of photocatalytic H_2 generation system was measured via employing the 300 W Xenon lamp equipped with the band-pass filter. The AQY was determined according to the following equations:

$$\begin{aligned} n_{\text{photons}} &= t \times \frac{P\lambda}{hc} \\ \text{AQY}(\%) &= \frac{\text{number of reacted electrons}}{\text{number of incident electrons}} \times 100 \\ &= \frac{2 \times \text{number of evolved H}_2 \text{ molecules}}{\text{number of incident electrons}} \times 100 \end{aligned}$$

where P , λ , h , c and t are the incident light power, wavelength of incident light, Planck's constant, velocity of light and illumination time, respectively. The power of incident light was detected by the optical power meter.

2.3. Photocatalytic CO_2 reduction

The visible-light driven photocatalytic CO_2 reduction experiments were carried out in the closed circulation reactor system with the top-window Pyrex cell. The reaction temperature was controlled at 20°C through circulation of cooling water. A 300 W Xenon lamp equipped with a 420 nm cut-off filter was placed on top as the light source. The photocatalyst (50 mg) was dissolved into 5 mL of deionized water. Before the photoreaction was started, the reactor was evacuated and refilled with high-purity CO_2 (SOXAL, 99.999%) several times to get rid of the air inside. Then the CO_2 gas was filled into the reactor to reach a pressure of 650 torr. The gaseous products at different reaction time were detected by an online gas chromatograph (Agilent 7890a, Hayesep Q 80–100 column).

3. Results and discussions

3.1. Structure, morphology and chemical states

The crystal phase and crystallographic structure of the prepared samples were probed using XRD, and the representative XRD patterns of $\text{Zn}_x\text{In}_2\text{S}_{3+x}$ samples are shown in Fig. 1. It is clear that the $\text{Zn}_x\text{In}_2\text{S}_{3+x}$ samples all display similar XRD patterns. The peaks at 21.6° , 26.8° , 28.1° , 47.0° , 52.2° and 55.9° can be indexed as (006), (102), (104), (112), (1012) and (202) facets, respectively, indicating that the XRD peaks of $\text{Zn}_x\text{In}_2\text{S}_{3+x}$ samples can be assigned to the hexagonal phase [25]. No other impurities, for example, oxides, binary sulfides, or organic compounds related to the reactants, were detected via the XRD analysis, indicating phase purity of the prepared $\text{Zn}_x\text{In}_2\text{S}_{3+x}$ samples. As reported by Anagnostopoulos et al., all $\text{Zn}_x\text{In}_2\text{S}_{3+x}$ phases included m layers of $-\text{S}\text{Zn}\text{S}-$ and the repeating structural unit $-\text{SIn}(o)\text{SIn}(t)\text{S}\square\text{S}-$,

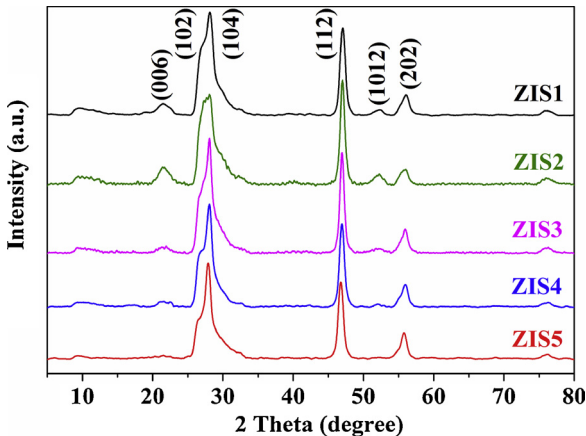


Fig. 1. X-ray diffraction patterns of $\text{Zn}_x\text{In}_2\text{S}_{3+x}$ samples.

with indium layers in the octahedral (o) and tetrahedral (t) sites and a layer with the vacant (\square) cationic sites [26]. Although chemical compositions of these samples were different, they were similar in some structural characteristics, thus resulting in similar XRD patterns. It should be noted that, in some cases, the corresponding intensities of some diffraction peaks in the XRD patterns of these products were different. For example, the intensities of the (006) and (1012) peaks became weaker but the intensity of the (104) peak became stronger for the $\text{Zn}_x\text{In}_2\text{S}_{3+x}$ samples as x increased from 1 to 5. This difference could be attributed to the dissimilarity in - $\text{S}\text{Zn}\text{S}$ - layers and composition faults in the layered crystals.

Fig. 2 displays the morphology information and microscopic structure of synthesized $\text{Zn}_x\text{In}_2\text{S}_{3+x}$ samples. From Fig. 2(a), it is obvious that the microsphere structure of the ZIS1 sample was composed of cross-linked nanosheets, and the average diameter of the microspheres was about $2\text{--}3 \mu\text{m}$. All microspheres were composed of numerous petals/sheets upon closer observation. This growth tendency of layered structures may be related to the lamellar feature of hexagonal ZIS1 [27]. ZIS2, ZIS3 and ZIS4 also showed microsphere structures with diameters in the range of $2\text{--}3 \mu\text{m}$ and comprised of petals/sheets (Fig. 2(b-d)), but the petals/sheets in the microspheres were thicker, which may be due to the increased - $\text{S}\text{Zn}\text{S}$ - layers (and composition faults in layered crystals). As x increased to 5, the shapes of microspheres for ZIS5 were partially distorted. EDS-mapping analysis, which was also carried out in order to further clarify the composition profile of the prepared ZIS1, shows that Zn, In and S elements were distributed uniformly. In addition, TEM and HRTEM analyses were used to study the microstructure of ZIS1. The TEM images of the as prepared ZIS1 in Fig. 2 (g, h) indicate that the sample comprised of relatively uniform sphere-like slightly aggregated ZnIn_2S_4 structures, with each sphere containing numerous two-dimensional petals, which is consistent with the SEM results (Fig. 2(a)). The high-resolution TEM (HRTEM) image of ZIS1 sample is shown in Fig. 2(i). It is clear that the lattice fringe spacing is 0.32 nm , corresponding to the (102) crystal plane of ZIS1 sample, which is in agreement with the XRD pattern (Fig. 1).

X-ray photoelectron spectroscopy (XPS) measurements were performed to further clarify the chemical states and surface composition of the prepared ZIS1 sample, as presented in Fig. 3. The survey spectrum in Fig. 3(a) shows that the Zn, In, S, O and C elements were all present in the ZIS1 sample. Among these, the O-1 s and C-1 s were inevitably present mainly due to exposure of the ZIS1 sample material in air, resulting in the absorption of the gaseous molecules. The high-resolution spectra of In, Zn and S are displayed in Fig. 3(b-d). Fig. 3(b) shows that the high-resolution spectra of S 2p has two peaks at 161.4 eV (S 2p $3/2$) and 162.6 eV (S 2p $1/2$), both of which corresponded to S^{2-} [28]. As for the In 3d XPS spectrum (Fig. 3(c)), the two peaks at 444.9 eV (In 3d $5/2$) and 452.4 eV (In 3d $3/2$) suggests that the valence state of the indium

element was +3 [29,30]. The XPS spectrum of Zn 2p in Fig. 3(d) has two independent peaks at 1022.3 eV and 1045.4 eV , assigned to Zn^{2+} 2p $3/2$ and 2p $1/2$, respectively, indicating that the Zn species were present as Zn^{2+} [31]. From the XPS analysis (Table S2), the molar ratios of Zn:In:S in the prepared samples were shown to be 1.06:2:3.92, 2.04:2:4.90, 3.04:2:5.92, 4.04:2:6.82 and 5.02:2:7.84 for ZIS1, ZIS2, ZIS3, ZIS4 and ZIS5, respectively, which is close to the stoichiometric composition. Furthermore, the XRD, SEM, TEM as well as XPS results demonstrate that all of the $\text{Zn}_x\text{In}_2\text{S}_{3+x}$ ($x = 1\text{--}5$) layered crystals were successfully synthesized.

The BET specific surface area as well as pore-size distribution of the prepared $\text{Zn}_x\text{In}_2\text{S}_{3+x}$ samples were measured by nitrogen adsorption-desorption analysis. As displayed in Fig. 4, the nitrogen adsorption-desorption isotherm curves of all the $\text{Zn}_x\text{In}_2\text{S}_{3+x}$ samples displayed IV type adsorption isotherms with the typical H3 hysteresis loop according to the IUPAC classification, suggesting that the prepared $\text{Zn}_x\text{In}_2\text{S}_{3+x}$ samples were mesoporous [32]. The SEM and TEM images show that the mesoporous structure of the $\text{Zn}_x\text{In}_2\text{S}_{3+x}$ samples mainly originated from the loose stacking of the two-dimensional nanosheets and the assembled microspheres. The BET specific surface areas of the ZIS1, ZIS2, ZIS3, ZIS4 and ZIS5 samples were 57.57, 38.78, 57.82, 35.76 and $33.82 \text{ m}^2/\text{g}$, respectively. In addition, Fig. S1 shows that the synthesized $\text{Zn}_x\text{In}_2\text{S}_{3+x}$ samples had similar pore-size distributions, and the average pore diameters of ZIS1, ZIS2, ZIS3, ZIS4 and ZIS5 samples were about 15.63, 6.55, 11.98, 9.94 and 9.76 nm, respectively, which supplied efficient transport pathways for product molecules and reactant. It can be deduced that the photocatalytic activity of the prepared $\text{Zn}_x\text{In}_2\text{S}_{3+x}$ samples was not directly related to the BET specific surface area from the subsequent activity results.

3.2. Photocatalytic performance of various composition faults in $\text{Zn}_x\text{In}_2\text{S}_{3+x}$

3.2.1. Photocatalytic H_2 generation

The hydrogen evolution experiments were carried out under visible light irradiation in order to evaluate the photocatalytic performance of the prepared photocatalysts. In order to boost the photocatalytic H_2 evolution, a certain amount of platinum (Pt) was loaded as a cocatalyst on the photocatalyst to provide active sites for H_2 production. The control experiments showed no significant H_2 was produced in the absence of either irradiation or photocatalyst, suggesting the H_2 evolution was a photo-driven catalytic reaction. Fig. 5(a) displays the photocatalytic activities of the $\text{Zn}_x\text{In}_2\text{S}_{3+x}$ samples for H_2 evolution from water under visible light irradiation through applying 15%TEOA as the sacrificial reagent. It is clear the photocatalytic activities of $\text{Zn}_x\text{In}_2\text{S}_{3+x}$ samples strongly depended upon the value of x . When $x = 0$, the obtained In_2S_3 photocatalyst exhibited negligible hydrogen production rate ($33.6 \text{ }\mu\text{mol}\cdot\text{h}^{-1}\text{ g}^{-1}$). The obtained ZIS1 sample showed the best photocatalytic activity, with the hydrogen production rate determined to be $2.93 \text{ mmol}\cdot\text{h}^{-1}\text{ g}^{-1}$. However, the activities of the $\text{Zn}_x\text{In}_2\text{S}_{3+x}$ samples decreased when $x \geq 2$. Specifically, the average H_2 evolution rates of the prepared ZIS2, ZIS3, ZIS4 and ZIS5 samples were 2.86 , 2.32 , 2.15 and $2.05 \text{ mmol}\cdot\text{h}^{-1}\text{ g}^{-1}$, respectively. Thus, we hypothesize that the different photocatalytic activities mainly stemmed from the modulation effect of composition faults in the internal charge carrier transfer of the $\text{Zn}_x\text{In}_2\text{S}_{3+x}$ layered crystals.

Furthermore, the photocatalytic activity of $\text{Zn}_x\text{In}_2\text{S}_{3+x}$ samples under the full-spectrum light irradiation was studied through using the 300 W Xe lamp. As displayed in Fig. 5(b), the photocatalytic H_2 evolution system under irradiation of full-spectrum light displayed a much higher H_2 production rate as compared with that under irradiation of visible light, which corresponds to the contribution of ultraviolet light irradiation. As shown in Fig. 5(b), the H_2 evolution rate for the as-obtained $\text{Zn}_x\text{In}_2\text{S}_{3+x}$ samples was the highest for ZIS1 at $7.33 \text{ mmol}\cdot\text{h}^{-1}\text{ g}^{-1}$, followed by ZIS2 ($5.76 \text{ mmol}\cdot\text{h}^{-1}\text{ g}^{-1}$), ZIS3 ($3.62 \text{ mmol}\cdot\text{h}^{-1}\text{ g}^{-1}$), ZIS4 ($3.42 \text{ mmol}\cdot\text{h}^{-1}\text{ g}^{-1}$) and ZIS5

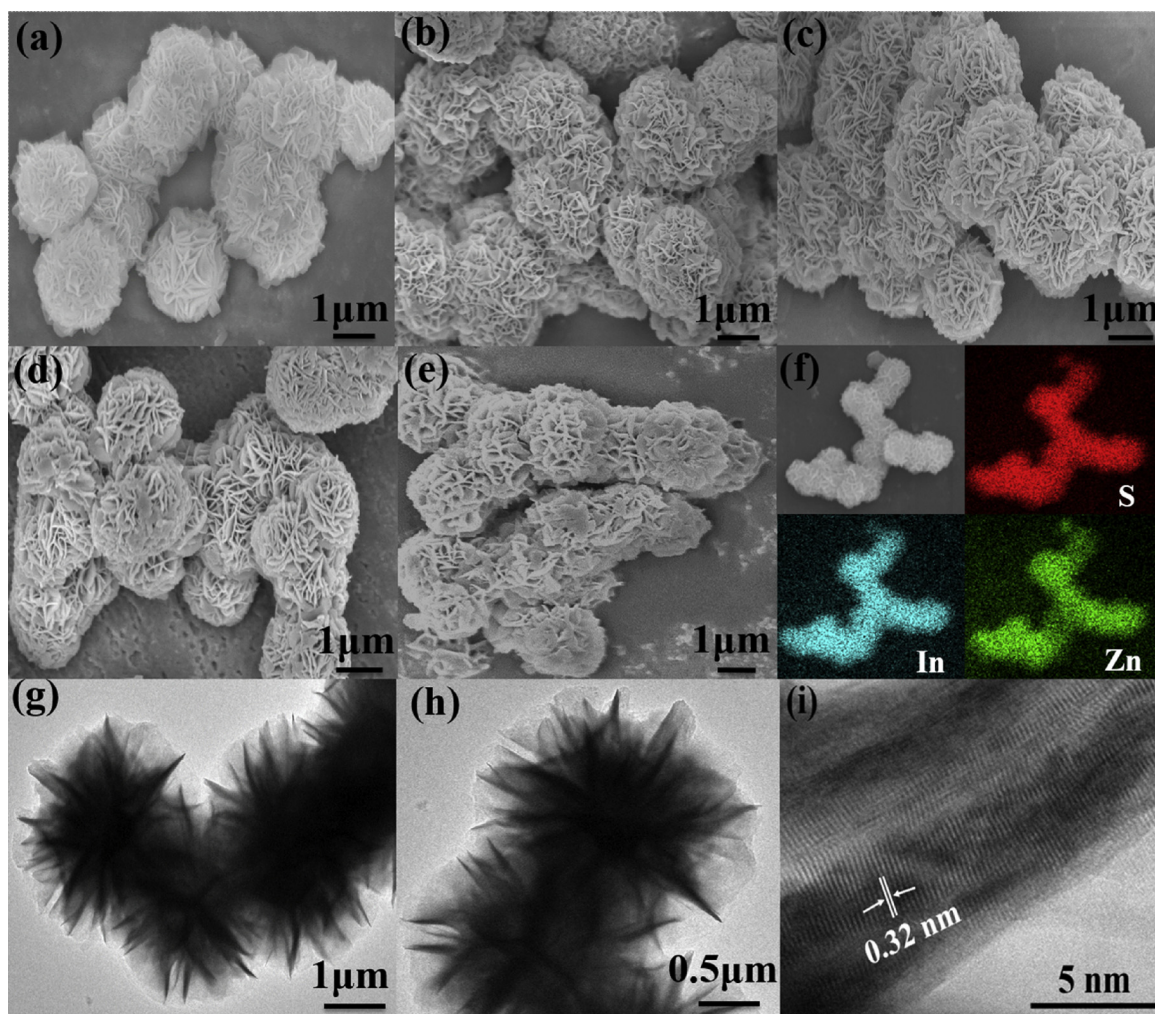


Fig. 2. SEM images of ZIS1 (a), ZIS2 (b), ZIS3 (c), ZIS4 (d) and ZIS5 (e), as well as EDS elemental mapping analysis of the ZF1 sample (f); TEM (g, h) and HRTEM (i) images of ZIS1 sample.

($3.06 \text{ mmol}\cdot\text{h}^{-1} \text{ g}^{-1}$).

It is well known that Pt nanoparticles are a highly efficient H₂ evolution reaction catalyst and have been widely used as an effective cocatalyst to boost the photocatalytic H₂ production activity of semiconductor photocatalysts [33–35]. For comparison, the Pt-loaded ZIS1 photocatalysts prepared via an in-situ photo-deposition method was investigated under the same reaction conditions. As displayed in Fig. 5(c), the optimal amount of Pt loaded on ZIS1 photocatalyst was determined to be 2 wt%, which gave a photocatalytic H₂ generation rate of $2.93 \text{ mmol}\cdot\text{h}^{-1} \text{ g}^{-1}$. In detail, the photocatalytic average H₂ generation rates of the samples were 0.17, 1.81, 2.52 and $1.59 \text{ mmol}\cdot\text{h}^{-1} \text{ g}^{-1}$ for the Pt/ZIS1 with respectively 0 wt%, 1 wt%, 3 wt% and 5 wt% of Pt. Therefore, 2 wt% Pt photo-deposited on the Z_xIn₂S_{3+x} samples gave optimal efficiency of water splitting to generate hydrogen in the present study.

Fig. 5(d) displays photocatalytic H₂ generation as a function of holes scavenger (TEOA) concentrations, which suggests that the H₂ generation rate gradually increased with TEOA concentration up to 15% by volume of TEOA (i.e., 15 mL in 100 mL of mixed solution). The decrease in H₂ generation rate at higher TEOA concentrations ($> 15\%$ by volume) may be due to the high viscosity and multiple molecules in the reaction medium reducing the light-harvesting capacity of the nano-composites [36]. In detail, the photocatalytic H₂ generation rates of the ZIS1 sample on different amount of TEOA concentrations is 0.08, 1.39, 2.38, 2.93 and $1.95 \text{ mmol}\cdot\text{h}^{-1} \text{ g}^{-1}$ for 0%, 5%, 10%, 15% and 20% (v/v), respectively. Therefore, 15% (v/v) TEOA was the best hole

scavenger concentration for efficient water splitting to generate hydrogen in the present study.

3.2.2. Photocatalytic CO₂ reduction

The photocatalytic CO₂ reduction reaction of Z_xIn₂S_{3+x} samples was carried out in the presence of water vapor and the results are shown in Fig. 6. For all the photocatalysts evaluated, CO is the main product and H₂ was not detected. As displayed in Fig. 6, CO₂ can be reduced to CO via water vapor over all Z_xIn₂S_{3+x} samples, because the conducting band (CB) edge of Z_xIn₂S_{3+x} samples was in range of $-1.08\text{--}1.21 \text{ eV}$ (vs normal H₂ electrode, NHE), which is much more negative than E°(CO/CO₂) ($\text{CO}_2 + 2\text{e}^- + 2\text{H}^+ \rightarrow \text{CO} + \text{H}_2\text{O}$, E°_{redox} = -0.53 V vs NHE). Obviously, the CO generation rate gradually decreased as x increased from 1 to 5. Fig. 6 reveals that the ZIS1 sample exhibited the highest CO formation rate of $40.4 \text{ } \mu\text{mol}\cdot\text{h}^{-1} \text{ g}^{-1}$, followed ZIS2, ZIS3, ZIS4 then ZIS5 at 33.0, 17.4, 6.2 and $4.4 \text{ } \mu\text{mol}\cdot\text{h}^{-1} \text{ g}^{-1}$, respectively. Blank experiments, in the absence of a photocatalyst under visible light irradiation as well as in the dark using the ZIS1 sample under identical experimental conditions, showed that there was negligible CO productivity. Furthermore, control experiments using argon gas instead of CO₂ gas under the same experimental conditions resulted in no detectable amount of CO.

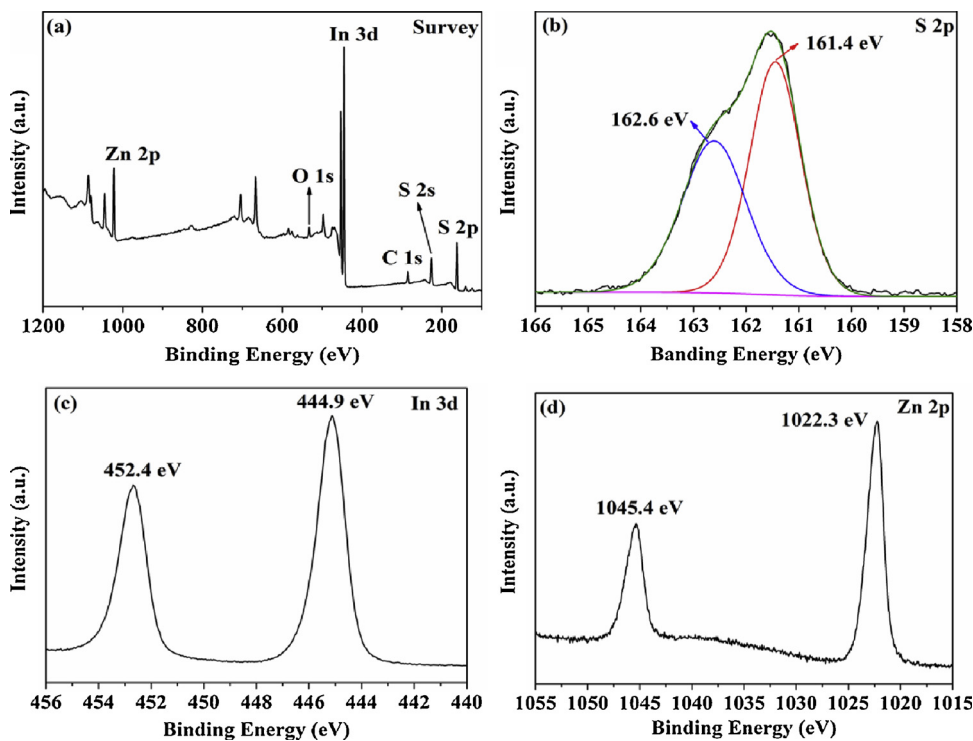


Fig. 3. XPS spectra of the ZIS1 sample: (a) survey, (b) S 2p, (c) In 3d and (d) Zn 2p.

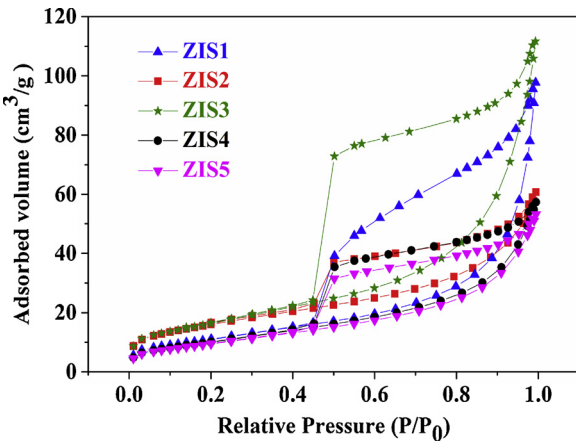


Fig. 4. Nitrogen adsorption-desorption isotherms of $Z_{nx}In_2S_{3+x}$ samples.

3.3. The modulating action of various composition faults of $Z_{nx}In_2S_{3+x}$ in optical absorption and photoelectrochemical properties

3.3.1. I-V characteristics

As shown in Fig. 7, the I-V relationships were linear for these $Z_{nx}In_2S_{3+x}$ semiconductors for small values of applied voltage in the range of 0~1 V. All these $Z_{nx}In_2S_{3+x}$ materials exhibited high values of resistivity, with the ZIS1 sample being the most conductive. It provides proof of the existence of extended composition faults acting as energy barriers between the layers of ZIS1 appears to be responsible for conductivity. Similar conclusions have also been shown in previous research [24,37].

3.3.2. Optical property

The optical absorption property of $Z_{nx}In_2S_{3+x}$ samples was studied by UV-vis diffuse reflectance spectroscopy (DRS), as displayed in Fig. 8(a). These $Z_{nx}In_2S_{3+x}$ samples exhibited a strong absorption band with a steep edge in the visible light region, which suggests that the

visible light absorption was owed to the band gap transition, instead of the transition from impurity levels to the conduction band (CB) of $Z_{nx}In_2S_{3+x}$ as observed from the metal-ion doped ZnS photocatalysts [38,39]. As the value of x increased from 1 to 5, the absorption edges of the $Z_{nx}In_2S_{3+x}$ samples shifted to shorter wavelength, suggesting the band gap of $Z_{nx}In_2S_{3+x}$ widened monotonically with increasing molar ratio of Zn to In. Particularly, the ZIS1 sample owned the absorption edges of longest wavelengths compared to the other ZIS samples. Thus, the composition faults weakly changed the solar absorption properties. Moreover, the energy band-gap values of $Z_{nx}In_2S_{3+x}$ samples can be estimated via employing the Kubelka-Munk function [40]:

$$\alpha h \nu = A (h \nu - E_g)^{n/2}$$

where α , h , ν , E_g and A are the absorption coefficient, Planck constant, light frequency, band gap energy and a constant, respectively. As displayed in Fig. 8(b), the E_g values of ZIS1, ZIS2, ZIS3, ZIS4 and ZIS5 samples were calculated to be 2.65, 2.73, 2.76, 2.79 and 2.84 eV, respectively. In addition, VB-XPS was used to further investigate the properties of the band structure [41]. As displayed in Fig. 8(c), the maximum valence band of ZIS1, ZIS2, ZIS3, ZIS4 and ZIS5 samples were determined to be 1.57, 1.59, 1.59, 1.61 and 1.63 eV, respectively. Considering the band gap energies presented in Fig. 8(b), the conducting band positions of ZIS1, ZIS2, ZIS3, ZIS4 and ZIS5 samples were calculated to be -1.08, -1.14, -1.17, -1.18 and -1.21 eV, respectively, according to the empirical formula: $E_{VB} = E_{CB} + E_g$ [42]. Based on the above data and analysis, the band structures of the ZIS1, ZIS2, ZIS3, ZIS4 and ZIS5 samples are depicted in Fig. 8(d). Therefore, the composition faults weakly affected the band structure of $Z_{nx}In_2S_{3+x}$ with less visible light absorption.

In addition, the recombination rates of the photoinduced electron-hole pair were detected via photoluminescence emission spectra (PL) [43]. Fig. 9(a) compares the PL emission spectra of the different $Z_{nx}In_2S_{3+x}$ samples detected at an excitation wavelength of 325 nm. As shown in Fig. 9(a), the PL intensity for the obtained $Z_{nx}In_2S_{3+x}$ samples was the lowest for ZIS1, followed by ZIS2, ZIS3, ZIS4, then ZIS5. Generally speaking, the stronger the intensity of the PL spectrum is, the

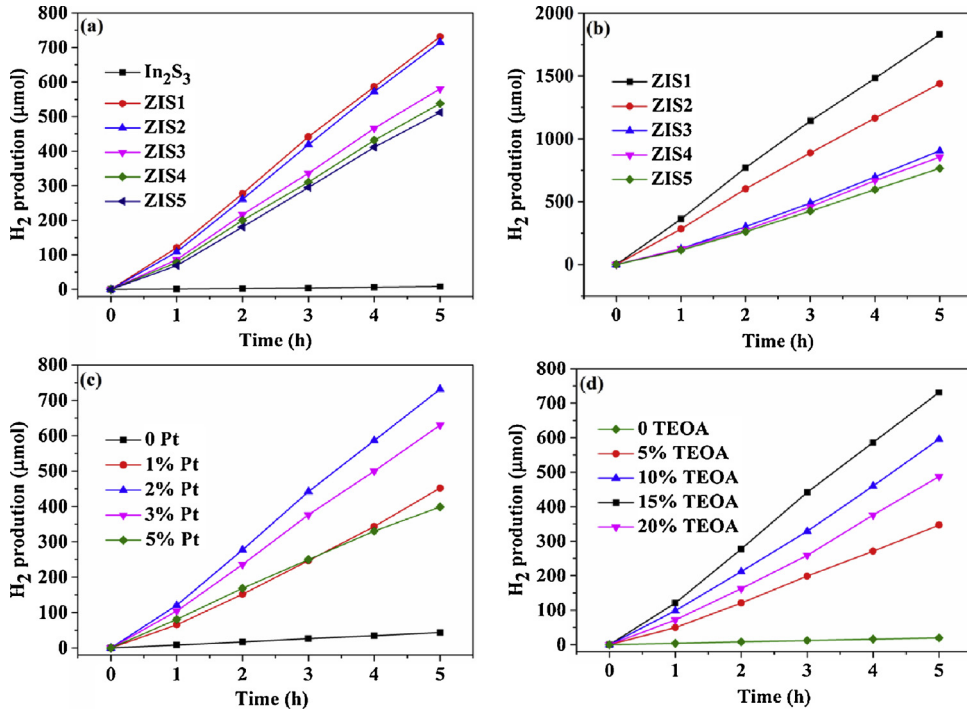


Fig. 5. Evolution of H₂ with time over Zn_xIn₂S_{3+x} samples under a 300 W Xe lamp equipped with (a) or without (b) a 420 nm cutoff filter; (c) effect of different amounts of Pt and (d) effect of different concentrations of sacrificial agent (TEOA) on the photocatalytic H₂ evolution by ZIS1.

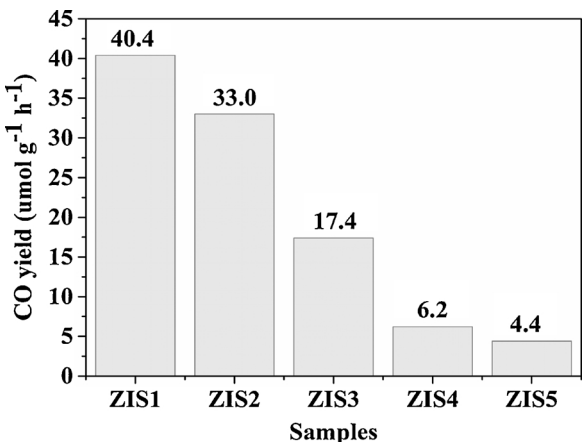


Fig. 6. Photoreduction of CO₂ into CO under visible light irradiation for the Zn_xIn₂S_{3+x} samples.

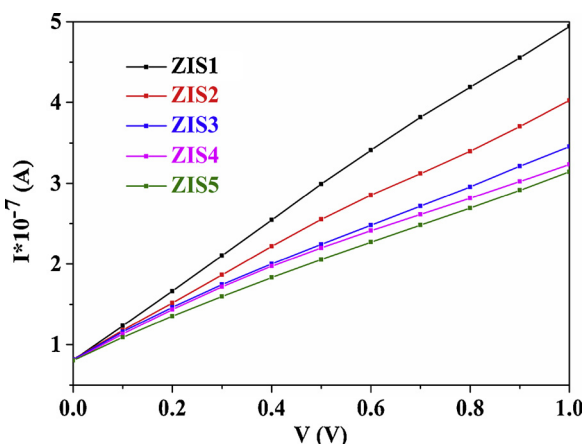


Fig. 7. I-V characteristics of Zn_xIn₂S_{3+x} samples.

faster the recombination rate of electrons and holes is, and thus the lower the photocatalytic activity is. Obviously, ZIS1 had the weakest PL intensity than those of the other prepared samples, which suggests the lowest photo-generated electron–hole pair recombination rate. This was because the composition faults acted as energy barriers to block the photoinduced electron transfer between the layers of ZnIn₂S₄, easing the recombination of electron–hole pairs.

Furthermore, the efficiency of radiative recombination of the photoinduced charge carriers was characterized by time-resolved fluorescence decay spectra. As displayed in Fig. 9(b), the fluorescence peak decay of the obtained ZIS1 sample was slowest among all the Zn_xIn₂S_{3+x} samples at a lifetime of 2.074 ns, followed by ZIS2, ZIS3, ZIS4 and ZIS5 at 1.887, 1.856, 1.620 and 0.946 ns, respectively. The longest lifetime of the ZIS1 sample relative to that of other Zn_xIn₂S_{3+x} samples indicates that the lifetime of photo-generated charge carriers was prolonged, and the most efficient separation of electrons and holes in the ZIS1 sample stemmed from the higher conductive properties, and thus increased the possibility of charge carriers participating in the photocatalytic reaction.

3.3.3. Photoelectrochemical response

Photocurrent measurement was carried out to assess the separation efficiency of photogenerated electron–hole pairs for the photocatalytic performance. Fig. 10(a) displays the photocurrent-time curve of Zn_xIn₂S_{3+x} samples under visible-light irradiation for several on-off cycles. The photocurrent density increased sharply when the light was turned on, and immediately returned to its initial negligible value when the light was switched off. It is well known that photocurrent is generated via the diffusion electrons from separation of the electron–hole pairs produced by the visible light [44]. As shown in Fig. 10 (a), the ZIS1 sample exhibited the greatest photocurrent density among all the other samples. It is generally believed that the photo-generated hole–electron pairs are generated via visible light excitation of the photocatalyst. The photo-generated holes can be captured via the holes scavenger in the electrolyte, and the photocurrent is formed through the directional migration of photo-generated electrons. Therefore, it can be concluded that the ZIS1 sample generated more photo-generated hole–

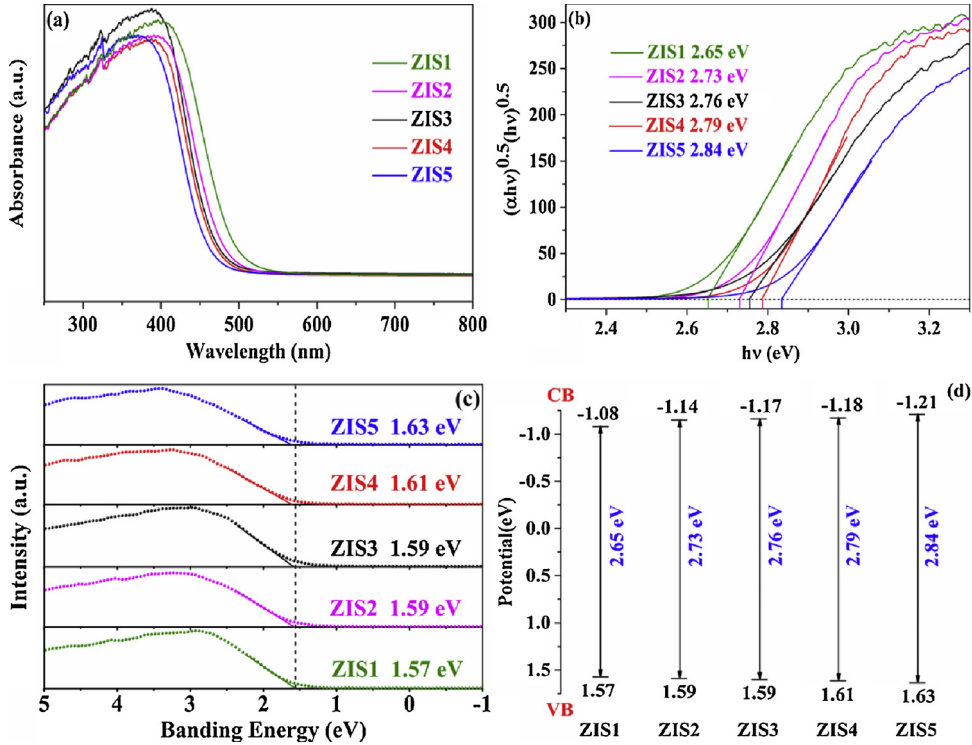


Fig. 8. (a) UV-vis diffuse reflectance spectra; (b) plot of $(\alpha h v)^{0.5}$ vs. $h v$ (photon energy); (c) valence-band XPS spectra and (d) band structure diagram of ZIS1, ZIS2, ZIS3, ZIS4 and ZIS5 samples.

electron pairs and prolonged the lifetime of photo-generated carriers. This also provides proof that the more conductive ZIS1 was, the more photoinduced electrons accumulated on the surface of ZIS1 due to the fast internal charge immigration. Additionally, electrochemical impedance spectroscopy (EIS) Nyquist plots can further investigate the separation and transfer efficiency of electron-hole pairs, and reflect the transfer resistance across the solid-liquid junction in the electrode-electrolyte interface region [45,46]. It can be seen from Fig. 10(b) that the EIS Nyquist plots of the ZIS1 sample has the smallest radius among all the $Zn_xIn_2S_{3+x}$ samples, suggesting that the ZIS1 sample exhibited the lowest resistance for electron transfer, and thus that the separation and transfer efficiency of photo-induced carriers for the ZIS1 sample was the fastest [47]. The electrochemical impedance spectroscopy results are consistent with the results of the photocurrent curves. From the analysis of I-V characteristics, optical absorption and photoelectrochemical properties, it can be concluded that the existence of composition faults affects the light absorption and photo-generated electron-hole separation of $Zn_xIn_2S_{3+x}$, which collectively impacts the photocatalytic reaction rate for hydrogen generation and CO_2 reduction.

3.4. Photocatalytic mechanism

The possible intrinsic defects present were directly measured by the electron spin resonance (ESR) technique with 2,2,6,6-Tetramethylpiperidinoxy (TEMPO). The experiments were carried out both under dark and visible light irradiation conditions. As indicated in Fig. 11 (a) and (b), the intensities of the peaks of the spin-trapped TEMPO- h^+ increased when exposed to visible light irradiation relative to that in the dark for the $Zn_xIn_2S_{3+x}$ samples. The characteristic signals at g-values (i.e., the spectral splitting factor) of 2.003 were detected for the $Zn_xIn_2S_{3+x}$ samples, corresponding to the electrons captured by the sulfur vacancies [21]. Furthermore, all the $Zn_xIn_2S_{3+x}$ samples possessed the similar ESR signals, and the ZIS1 product possessed obviously the strongest ESR intensity among all the $Zn_xIn_2S_{3+x}$ samples, corresponding to the highest concentration of sulfur vacancies formed in the system. The ESR signal intensity suggests the activity in producing vacancies followed the order: ZIS1 > ZIS2 > ZIS3 > ZIS4 > ZIS5. Moreover, the highest occupied molecular orbital (HOMO) levels of $Zn_xIn_2S_{3+x}$ are dependent on the hybridized orbitals of the S3p and Zn3d, while the hybridized In5s5p and S3p orbitals mainly determine

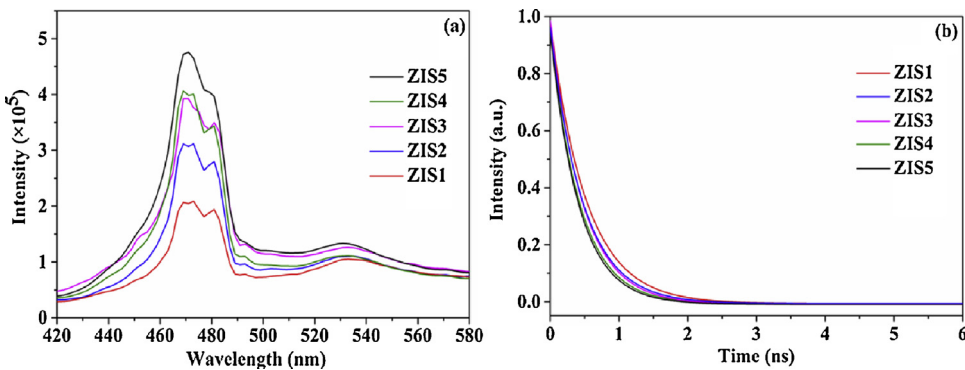


Fig. 9. (a) Photoluminescence (PL) spectra and (b) fluorescence lifetime of ZIS1, ZIS2, ZIS3, ZIS4 and ZIS5 samples at an excitation wavelength of 325 nm.

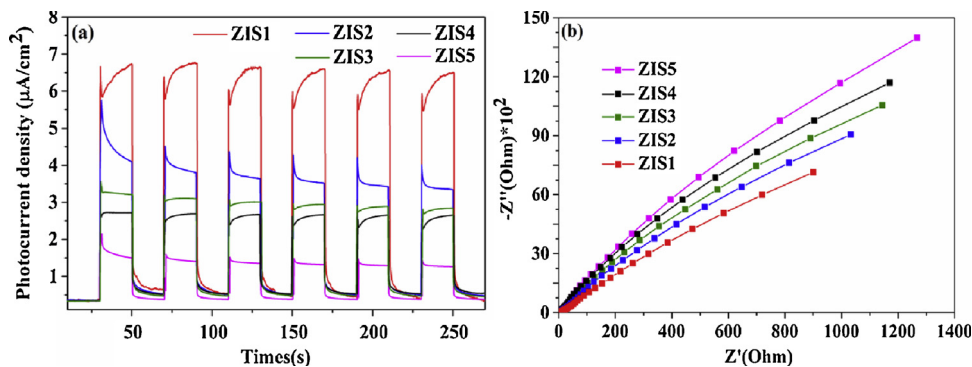


Fig. 10. (a) Transient photocurrent response and (b) EIS Nyquist plots of ZIS1, ZIS2, ZIS3, ZIS4 and ZIS5 samples under intermittent visible light irradiation.

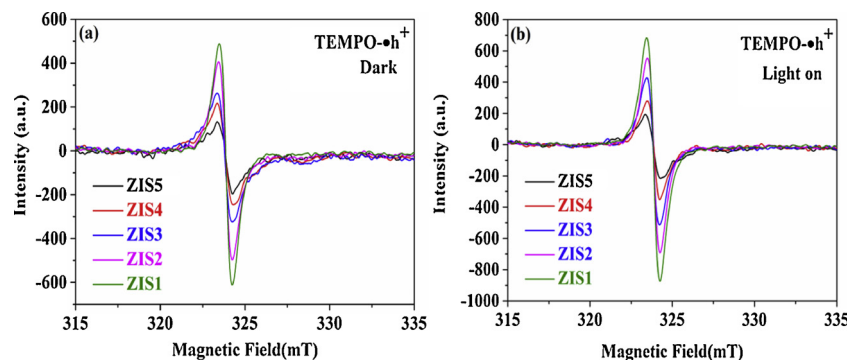


Fig. 11. ESR spectra of radical adducts trapped by TEMPO (h^+): in aqueous dispersion for TEMPO- h^+ of $\text{Zn}_x\text{In}_2\text{S}_{3+x}$ samples in the dark (a) and under visible light irradiation (b).

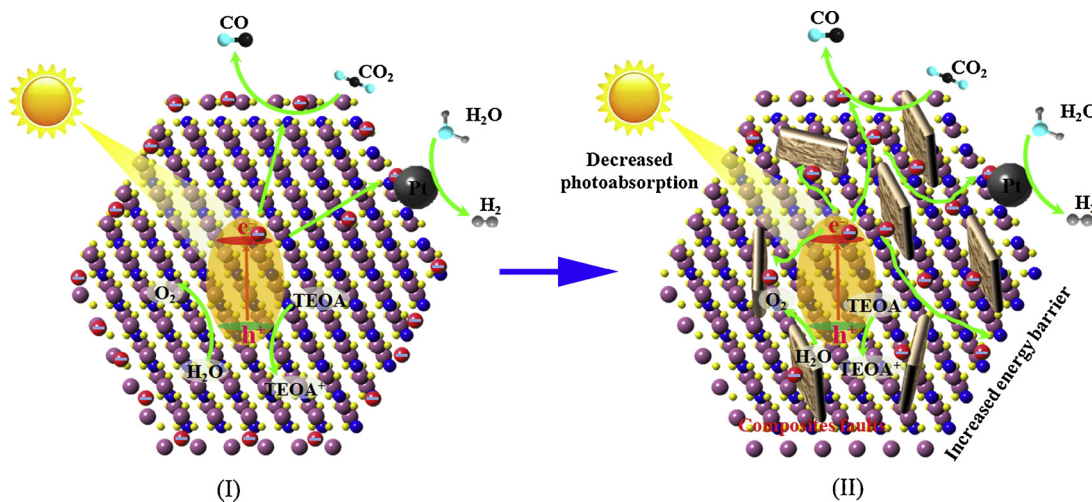


Fig. 12. Proposed mechanism of photocatalytic reaction in the absence (I) and presence (II) of composites faults.

the lowest unoccupied molecular orbital (LUMO) levels [16,20]. Under visible light irradiation, the electrons at HOMO levels were excited and jumped to the LOMO levels. After transferring to the external surface of photocatalyst, the photoredox reaction occurred.

The underlying mechanism proposed for effective photocatalytic H₂ generation of the ZIS1 sample is displayed in Fig. 12. The photo-generated electron-hole pairs are produced in the prepared ZIS1 sample under visible-light irradiation. Because of the lower Fermi level of noble metal Pt, the photo-excited electrons in the valence band can be transferred from conduction band to Pt nanoparticles photo-deposited on the surface of photocatalysts, while photo-generated holes remain. Therefore, the likelihood of electron-hole recombination is greatly decreased, leading to efficient charge separation and increased

photocatalytic activity [48]. The absence of composition faults makes the free charge carrier more easily transfer to the external surface of ZIS1. The photogenerated electrons in the solid-liquid interface are captured by H⁺ from H₂O to generate H₂, and the photo-generated holes are trapped via TEOA to form TEOA $^+$ in the photocatalytic process. However, the presence of composition faults produces an additional energy barrier, so that the transfer process of charged carrier is blocked, which lowers the photocatalytic reaction rate.

It is well known that, for a typical CO₂ photoreduction reaction, the main processes are namely: (i) photo-absorption; (ii) separation and transport of photo-generated carriers; and (iii) CO₂ adsorption and reduction via photo-excited electrons [49]. During the CO₂ photoreduction process, CO₂ adsorption is also generally considered to be another

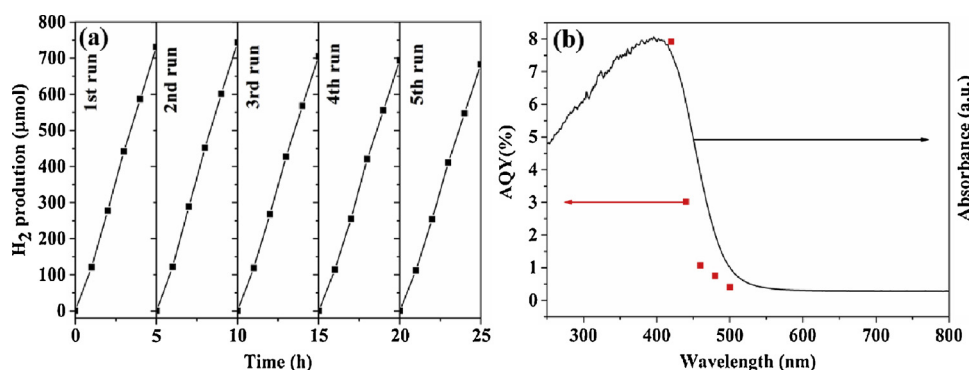


Fig. 13. (a) Photocatalytic H₂ evolution reactions by the ZIS1 sample under the visible-light irradiation over 5 cycles; (b) AQY and UV-vis absorption spectrum of ZIS1 sample.

prerequisite for the CO₂ photoreduction process. The negatively charged surface of ZIS enhances CO₂ adsorption on their surfaces [50]. Usually, water molecular can be employed as the electron donor and the proton source in the CO₂ reduction process, and therefore the intimate contact between water and photocatalyst is beneficial for CO₂ reduction. The photo-induced holes are eliminated by H₂O for O₂ formation. The surface hydrophilicity of ZIS1 facilitates more efficient external electron transfer to participate in the CO₂ reduction reaction.

3.5. Recyclability and stability

In addition to photocatalytic efficiency, the stability of the photocatalysts for recovery and reuse is also a key factor in measuring the quality of the photocatalysts. Photocatalytic reusability analysis was carried out to assess the catalytic stability of the ZIS1 sample up to five recycles (Fig. 13(a)). In order to study the durability of obtained photocatalysts, the photocatalytic H₂ generation reactions using the ZIS1 sample as the photocatalyst were carried out for 25 h with two intermediate evacuations after every 5 h of visible-light irradiation. As shown in Fig. 13(a), the photocatalytic H₂ evolution rates of 2.93, 2.97, 2.82, 2.78 and 2.73 mmol·h⁻¹ g⁻¹ were observed in the 1st, 2nd, 3rd, 4th and 5th runs, respectively, with the slight decrease in latter runs due to progressively reduced scavenger concentrations. The negligible loss of H₂ generation rate over five runs indicates the remarkable durability of the ZIS1 sample, making it a promising candidate for potential applications in sustainable energy conversion.

The apparent quantum yield (AQY) is another key parameter for evaluating the photocatalytic performance in addition to photocatalytic H₂ generation rate. Fig. 13(b) displays the UV-vis absorption spectrum of the ZIS1 sample along with the apparent quantum yield (AQY) of photocatalytic H₂ generation based on the ZIS1 sample as a function of the incident light wavelength. It is clear that the ZIS1 sample exhibited the highest AQY (7.92%) at the wavelength of 420 nm. The AQY values at 440, 460, 480 and 500 nm monochromatic light was determined to be 3.01%, 1.07%, 0.75% and 0.41%, respectively. As the irradiation wavelength increased, AQY decreased significantly, which is consistent with the UV-vis DRS of the ZIS1 sample, suggesting that the H₂ generation reaction was induced by the photons absorbed by the obtained ZIS1 sample.

4. Conclusions

Zn_xIn₂S_{3+x} ($x = 1\text{--}5$) with various composition faults were prepared by a simple hydrothermal method as a series of highly efficient visible-light-driven photocatalysts. Composition faults in the Zn_xIn₂S_{3+x} samples played important roles in internal charge transfer, further affecting the redox reactions of photogenerated electrons and holes. These Zn_xIn₂S_{3+x} samples had a controlled band gap and band structure, and the photocatalytic and optical properties were largely

dependent on the energy structure that varied with changing ratios of Zn to In. The ZnIn₂S₄ photocatalyst exhibited the highest activity for H₂ evolution, with a hydrogen generation rate of 2.93 mmol·h⁻¹ g⁻¹ and an apparent quantum yield at 420 nm of 7.92%. As for visible light-driven CO₂ reduction, the ZnIn₂S₄ sample also exhibited the highest CO formation rate of 40.4 μmol·h⁻¹ g⁻¹. This can be ascribed that the existence of composition faults that provided an extra energy barrier to block the photoinduced charge carrier transfer. In addition, the cycling experiments suggested excellent photostability, and thereby the synthetic Zn_xIn₂S_{3+x} samples are expected to be employable for long-term photocatalytic applications. Thus, this work provides a promising perspective to understand the structure-property relationship of Zn_xIn₂S_{3+x} layered crystals photocatalysts for highly efficient solar-to-fuels conversion.

Acknowledgments

The authors gratefully acknowledge the funding from the Singapore Ministry of Education Academic Research Funds Tier 2 (MOE2014-T2-2-074; ARC16/15) and Tier 1 (2015-T1-001-023; RG7/15), the GSK (GlaxoSmithKline) – EDB (Economic Development Board) Trust Fund, and the Joint Singapore-Germany Research Project Fund (SGP-PROG3-019).

Appendix A. Supplementary data

Supplementary material related to this article can be found, in the online version, at doi:<https://doi.org/10.1016/j.apcatb.2019.117810>.

References

- [1] J. Liu, Y. Liu, N. Liu, Y. Han, X. Zhang, H. Huang, Y. Lifshitz, S. Lee, J. Zhong, Z. Kang, *Science* 347 (2015) 970–974.
- [2] Y. Zheng, L. Lin, X. Ye, F. Guo, X. Wang, *Angew. Chem. Int. Ed.* 53 (2014) 1–6.
- [3] Y. Wang, H. Wang, F. Chen, F. Cao, X. Zhao, S. Meng, Y. Cui, *Appl. Catal. B: Environ.* 206 (2017) 417–425.
- [4] A. Fujishima, K. Honda, *Nature* 238 (1972) 37–38.
- [5] A. Weingarten, R. Kazantsev, L. Palmer, D. Fairfield, A. Koltonow, S. Stupp, *J. Am. Chem. Soc.* 137 (2015) 15241–15246.
- [6] D. Kim, D. Whang, S. Park, *J. Am. Chem. Soc.* 138 (2016) 8698–8701.
- [7] T. Stoll, M. Gennari, J. Fortage, C. Castillo, M. Rebarz, M. Sliwa, O. Poizat, F. dobel, A. Deronzier, M. Collomb, *Angew. Chem. Int. Ed.* 53 (2014) 1654–1658.
- [8] H. Wang, Y. Wu, X.Z. Yuan, G.M. Zeng, J. Zhou, X. Wang, J.W. Chew, *Adv. Mater.* 347 (2018) 1704561.
- [9] S.B. Wang, J.L. Lin, X.C. Wang, *Phys. Chem. Chem. Phys.* 16 (2014) 14656–14660.
- [10] X.H. Lin, Y.L. Gao, M. Jiang, Y.F. Zhang, Y.D. Hou, W.X. Dai, S.B. Wang, Z.X. Ding, *Appl. Catal. B Environ.* 224 (2018) 1009–1016.
- [11] Y. Wu, H. Wang, W.G. Tu, Y. Liu, S.Y. Wu, Y.Z. Tan, J.W. Chew, *Appl. Catal. B: Environ.* 233 (2018) 58–69.
- [12] Y. Wu, H. Wang, W.G. Tu, S.Y. Wu, Y. Liu, Y.Z. Tan, H.J. Luo, X.Z. Yuan, J.W. Chew, *Appl. Catal. B: Environ.* 229 (2018) 181–191.
- [13] D. Jiang, X. Chen, Z. Zhang, L. Zhang, Y. Wang, Z. Sun, R. Irfan, P. Du, *J. Catal.* 357 (2018) 147–153.
- [14] S.B. Wang, B.Y. Guan, X. Wang, X.W. Lou, *J. Am. Chem. Soc.* 140 (2018) 15145–15148.

- [15] S.B. Wang, B.Y. Guan, X.W. Lou, *J. Am. Chem. Soc.* 140 (2018) 5037–5040.
- [16] S.H. Shen, L. Zhao, L.J. Guo, *Int. J. Hydron. Energy* 35 (2010) 10148–10154.
- [17] L. Shang, C. Zhou, T. Bian, H.J. Yu, L.Z. Wu, C.H. Tung, T.R. Zhang, *J. Mater. Chem. A* 1 (2013) 4552–4558.
- [18] X.C. Jiao, Z.W. Chen, X.D. Li[†], Y.F. Sun, S. Gao, W.S. Yan, C.M. Wang, Q. Zhang, Y. Lin, Y. Luo, Y. Xie, *J. Am. Chem. Soc.* 139 (2017) 7586–7594.
- [19] H. Wang, H.L. Ye, B.H. Zhang, F.Q. Zhao, B.Z. Zeng, *J. Phys. Chem. C* 122 (2018) 20329–20336.
- [20] H. Wang, Y.M. Sun, Y. Wu, W.G. Tu, S.Y. Wu, X.Z. Yuan, G.M. Zeng, Z.C. Xu, S.Z. Li, J.W. Chew, *Appl. Catal. B: Environ.* 245 (2019) 290–301.
- [21] X. Li, Y. Cheng, Q.P. Wu, J. Xu, Y.S. Wang, *Appl. Catal. B: Environ.* 240 (2019) 270–276.
- [22] A.N. Anagnostopoulos, C. Manolikas, D. Papadopoulos, J. Spyridelis, *Phys. Stat. Sol. (a)* 72 (1982) 731–736.
- [23] N. Frangis, C. Manolikas, *Phys. Stat. Sol. (a)* 107 (1988) 589–595.
- [24] L.K. Gallos, A.N. Anagnostopoulos, P. Argyrakis, *Phys. Rev. B* 50 (1994) 14643–14646.
- [25] X.J. Ye, Y.H. Chen, Y.H. Wu, X.M. Zhang, X.C. Wang, S.F. Chen, *Appl. Catal. B: Environ.* 242 (2019) 302–311.
- [26] J.A. Kalomiros, A.N. Anagnostopoulos, J. Spyridelis, *Semicond. Sci. Technol.* 4 (1989) 536–542.
- [27] X. Gou, F. Cheng, Y. Shi, L. Zhang, S. Peng, J. Chen, et al., *J. Am. Chem. Soc.* 128 (2006) 7222–7229.
- [28] Z. Chen, Y.J. Xu, *ACS Appl. Mater. Interfaces* 5 (2013) 13353–13363.
- [29] C.W. Tan, G.Q. Zhu, M. Hojamberdiev, K.S. Lokesh, X.C. Luo, L. Jin, J.P. Zhou, P. Liu, J. Hazard. Mater. 278 (2014) 572–583.
- [30] S.B. Wang, B.Y. Guan, Y. Lu, X.W. Lou, *J. Am. Chem. Soc.* 139 (2017) 17305–17308.
- [31] Q. Liu, H. Lu, Z.W. Shi, F.L. Wu, J. Guo, K.M. Deng, L. Li, *ACS Appl. Mater. Interfaces* 6 (2014) 17200–17207.
- [32] C. Ling, X. Ye, J. Zhang, J. Zhang, S. Zhang, S. Meng, X. Fu, S. Chen, *Sci. Rep.* 7 (2017) 1–16.
- [33] L. Shang, B. Tong, H. Yu, G.I.N. Waterhouse, C. Zhou, Y. Zhao, M. Tahir, L.Z. Wu, C.H. Tung, T. Zhang, *Adv. Energy Mater.* 6 (2016) 1501241.
- [34] H. Wang, Y. Wu, M.B. Feng, W.G. Tu, T. Xiao, T. Xiong, H.X. Ang, X.Z. Yuan, J.W. Chew, *Water Res.* 144 (2018) 215–225.
- [35] T. Simon, M.T. Carlson, J.K. Stolarczyk, J. Feldmann, *ACS Energy Lett.* 1 (2016) 1137–1142.
- [36] P. Ravi, V.N. Rao, M.V. Shankar, M. Sathish, *Int. J. Hydrogen Energy* 43 (2018) 3976–3987.
- [37] A.N. Anagnostopoulos, *Phys. Stat. Sol. (a)* 75 (1983) 595–599.
- [38] A. Kudo, M. Sekizawa, *Catal. Lett.* 58 (1999) 241–243.
- [39] I. Tsuji, A. Kudo, *J. Photochem. Photobiol. A Chem.* 156 (2003) 249–252.
- [40] Y. Wu, H. Wang, Y.M. Sun, T. Xiao, W.G. Tu, X.Z. Yuan, G.M. Zeng, S.Z. Li, J.W. Chew, *Appl. Catal. B: Environ.* 227 (2018) 530–540.
- [41] Y. Wu, H. Wang, W.G. Tu, Y. Liu, Y.Z. Tan, X.Z. Yuan, J.W. Chew, J. Hazard. Mater. 347 (2018) 412–422.
- [42] D. Jing, L. Guo, *Catal. Commun.* 8 (2007) 795–799.
- [43] H. Wang, Y. Wu, T. Xiao, X.Z. Yuan, G.M. Zeng, W.G. Tu, S.Y. Wu, H.Y. Lee, Y.Z. Tan, J.W. Chew, *Appl. Catal. B: Environ.* 233 (2018) 213–225.
- [44] H.W. Han, X.Z. Zhao, J. Liu, J. Electrochem. Soc. 152 (2005) 164–A166.
- [45] N. Li, G. Liu, C. Zhen, F. Li, L.L. Zhang, H.M. Cheng, *Adv. Funct. Mater.* 21 (2011) 1717–1722.
- [46] Z. Hosseini, N. Taghavinia, N. Sharifi, M. Chavoshi, M. Rahman, *J. Phys. Chem. C* 112 (2008) 18686–18689.
- [47] X.Y. Zhang, H.X. Zhang, Y.Y. Xiang, S.B. Hao, Y.X. Zhang, R.N. Guo, X.W. Cheng, M.Z. Xie, Q.F. Cheng, B. Li, J. Hazard. Mater. 342 (2018) 353–363.
- [48] M. Ni, M.K.H. Leung, D.Y.C. Leung, K. Sumathy, *Renewable Sustainable Energy Rev.* 11 (2007) 401–425.
- [49] S. Qamar, F.C. Lei, L. Liang, S. Gao, K.T. Liu, Y.F. Sun, W.X. Ni, Y. Xie, *Nano Energy* 26 (2016) 692–698.
- [50] X.C. Jiao, Z.W. Chen, X.D. Li, Y.F. Sun, S. Gao, W.S. Yan, C.M. Wang, Q. Zhang, Y. Lin, Y. Luo, Y. Xie, *J. Am. Chem. Soc.* 139 (2017) 7586–7594.